A NUMERICAL ANALYSIS OF THE BRITISH EXPERIMENTAL ROTOR PROGRAM BLADE

Earl P.N. Duque
Research Scientist
U.S. Army Aeroflightdynamics Directorate – AVSCOM
Ames Research Center
Moffett Field, California 94035

FIFTEENTH EUROPEAN ROTORCRAFT FORUM

SEPTEMBER 12 - 15, 1989 AMSTERDAM

A NUMERICAL ANALYSIS OF THE
BRITISH EXPERIMENTAL ROTOR PROGRAM BLADE

Earl P.N. Duque
Research Scientist
U.S. Army Aeroflightdynamics Directorate - AVSCOM
Ames Research Center
Moffett Field, California 94035

1. Abstract

Two Computational Fluid Dynamic codes which solve the compressible full-potential and the Reynolds-Averaged Thin-Layer Navier-Stokes equations were used to analyze the non-rotating aerodynamic characteristics of the British Experimental Rotor Program (BERP) helicopter blade at three flow regimes: low angle of attack, high angle of attack and transonic. At low angle of attack, the BERP blade exhibited higher induced drag at a given lift as compared to other blade shapes such as rectangular, Puma, and a sweep-taper planform, but it had less induced drag than a 3:1 taper tip blade planform. Also, the computed spanwise loading at low angles of attack indicated a high leading edge suction peak at the blade notch and a drop in local lift coefficient at the sweep section of the blade. These characteristics provided a better understanding of the blades behavior at the other flow regimes. At high angle of attack, the blade attained high-lift by maintaining attached flow at the outermost spanwise locations. In the transonic regime, the BERP reduced the shock strength at the outer spanwise locations which reduced wave drag and shock-induced separation. Overall, the BERP blade exhibited many favorable aerodynamic characteristics in comparison to conventional helicopter rotor blades.

2. Introduction

Helicopters' inherent aerodynamic limitations prevent them from attaining high forward speed. For example, the Soviet Union's Hind A-10 held the helicopter world speed record of 228.9 mph (368.37 km/hr) for 8 years [1] until Westland Helicopter Ltd. flew their modified G-Lynx to 249.1 mph (400.87 km/hr) [2]. One of the significant differences between the Hind and the G-Lynx was the unique helicopter rotor blade known as the British Experimental Rotor Program (BERP) blade shown on the G-Lynx in figure 1.

Figure 1 - BERP Blade on the Westland G-Lynx

Westland attributes the improved forward flight rotor blade performance to the combination of unorthodox blade planform shape and high performance airfoils. This combination was designed to reduce transonic effects such as drag rise and increase rotor thrust by delaying retreating blade stall [2,3]. As shown in figure 2, the last 15% of the span was swept back to reduce transonic effects. However, simple swept tips shift the aerodynamic center behind the blade feathering axis which induces adverse control problems. To overcome this problem, leading-edge area was added to the swept tip region which formed the BERP blade's characteristic leading-edge notch. To further reduce the transonic effects at the tip, thin airfoil sections were used: 12% thick at the inboard sections, 8% at the sweep section and 6% at the extreme outboard sections.

To delay retreating blade stall, Westland incorporated a delta-wing-like planform at the extreme spanwise location; delta wings maintain high-lift at high angles of attack by forming a stable vortex structure over the wing surface. Secondly, high-lift airfoils developed by the Royal Aircraft Establishment [4] were used: RAE 9648, RAE 9645 and RAE 9634. The RAE 9645 is an aft loaded high-lift airfoil with a nose- down pitching moment. To counteract the 9645's pitching moment, the reflexed (nose- up pitching moment) RAE 9648 was used.

Westland designed the BERP blade with the use of extensive experimental data and some theoretical analysis. To date this data includes nonrotating wind tunnel experiments at low-speed, model rotor tests, and some flight experiments. As indicated by the world speed record of the G-Lynx, the flight tests have shown that the blade indeed improves rotor performance, but they do not fully explain either the aerodynamic behavior of the BERP blade or the blade's effect on the flow physics. Also, when Westland attained the world speed record, the helicopter industry realized that rotor blade performance could still be improved, but more detailed aerodynamic data was required to either improve upon the BERP blade design or to adopt it as a replacement rotor blade.

However, the cost and complexity of good detailed experiments limits the amount of available data on the BERP and many other advanced rotor blades. High equipment costs, modeling costs, the lack of available wind tunnel facilities, and the limited amount of man hours available for projects all contribute to the high costs of experiments. Also, the constantly
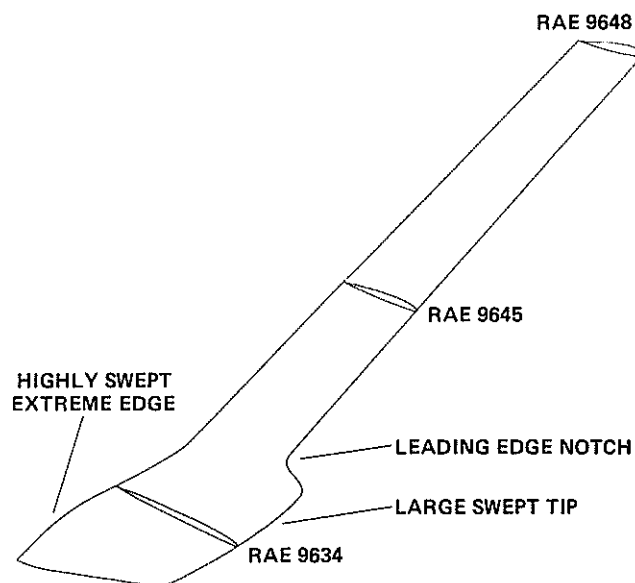
Figure 2 - BERP blade geometric features

varying flow environment of a rotor blade complicates obtaining detailed aerodynamic data. As an illustration, for a helicopter in forward flight, the advancing rotor blade travels at speeds high enough to cause shocks to form at the rotor blade tips. The retreating blade, on the other hand, operates at high angles of attack and low-speeds which can cause stall. Therefore, other methods, such as Computational Fluid Dynamics (CFD), are needed to complement experimental data on advanced rotor blades.

Within recent years, supercomputers such as the Cray 2 and Y-MP at NASA Ames Research Center's Numerical Aerodynamic Simulation Facility and the availability of more efficient numerical algorithms have made CFD a feasible research tool. By using CFD, one can model the flow field of a helicopter blade at different operating flow conditions and obtain highly detailed data. Currently, CFD methods cannot adequately model the inherently complex wake structure in helicopter rotor flows. Hence, extensive flow parametric studies using CFD are currently limited to nonrotating computations.

The main objective of this paper is to use CFD methods to develop a better understanding of the fundamental aerodynamic properties of the BERP blade. To accomplish this goal, a cooperative research agreement between Westland Helicopters Limited and the U.S. Army Aeroflightdynamics Directorate (AFDD) was established. Under this agreement, Westland performed nonrotating wind tunnel experiments while AFDD used the computer simulation capabilities at NASA Ames to simultaneously predict the Westland experiment. The wind tunnel tests performed by Brocklehurst of Westland Helicopters Ltd. [5] modeled the outermost 30% span of an otherwise full-scale model of the production BERP blade tip. Flow visualization and pressure data were obtained on a range of angle of attack sweeps from 0° to 22° with and without boundary layer trips. This paper presents the computational effort performed by the author which was designed to complement Westland's experiment and to provide industry additional data on this unique rotor blade.

3. Methodology

3.1 Computational Fluid Dynamic Methods

In CFD, there exists a hierarchy of methods which vary in computational cost and physical flow approximations. Basically, CFD methods compute the flow field around a body by solving a system of nonlinear equations that satisfy the basic physical laws of conservation of mass, momentum, and energy. These methods may be divided into two categories - inviscid and viscous. Inviscid computational methods simulate the fluid flow by assuming that the viscous effects of the fluid are negligible and can be ignored where as viscous computational methods maintain the viscous effects of the fluid.

The compressible full-potential rotor code by Strawn [6] called FPR, was chosen for the inviscid computations. The main advantage of this code is its relatively low computation cost per solution. For example, fully converged BERP blade solutions required approximately 20 minutes of CPU time on a Cray 2 supercomputer. However, this approach is limited to unseparated flows, since flow separation is a viscous effect of the fluid, and to flows that do not develop strong shock waves which violate the isentropic assumption in the full-potential formulation.

The FPR code solves the fully conservative unsteady full-potential equation in generalized coordinates with an Approximate Factorization method that is first-order backward differenced in time and second-order central differenced in space. Streamwise flux terms use upwind density biasing in regions of supercritical flow to ensure stability of the algorithm. The code imposes the freestream velocity field onto the blade by modifying the time-metric terms which effectively moves the blade through still air. Angles of attack are imposed by tilting the grid about the quarter chord relative to the nontilted root chord then modifying the time-metric

terms as before. At the radial outer grid boundary, a nonreflection boundary condition prevents wave reflections from affecting the solution while a freestream boundary condition is used at the outer spanwise grid location. The inboard plane boundary condition comes from the time derivative of the spanwise grid motion [6].

Of the various viscous codes available, the Reynolds-Averaged Thin-Layer Navier-Stokes code of Obayashi [7] known as LANS3D was used. Unlike the previous inviscid approach, this method can model separated flows, vortex dominated flows and flows with strong shock waves. However, this method is computationally expensive. The computations for this study required approximately 20 to 30 CPU hours per solution on the Cray 2. This high cost is a function of the high number of grid points needed, the number of equations or computer operations and the complexity of the flow phenomena.

The LANS3D code solves the three-dimensional (3-D) Reynolds-Averaged Thin Layer Navier-Stokes equations with the LU/ADI method of Obayashi [7]. The Thin-Layer form of the Navier-Stokes equations ignores the streamwise and spanwise stress terms of the full Navier-Stokes equations, and retains only those normal to the surfaces. The Reynolds stresses that result from time averaging the high-frequency turbulent fluctuations inherent in turbulent flows are modeled with the algebraic Baldwin-Lomax turbulence model. The resulting equations are then solved using the LU/ADI scheme which decomposes the block tridiagonal form of the Beam-Warming algorithm into the product of an upper and lower bidiagonal matrix along each coordinate direction by using a flux-vector splitting technique and similarity matrix transformations. This decomposition allows for the efficient solution of the Navier-Stokes equations.

Previously, the FPR code has been used to investigate the performance of rotating helicopter rotor blades of simple planform shape. The code has been validated with experimental data and is very robust. The LANS3D code has been used in transonic fixed-wing and low-speed delta-wing computational studies. It is also robust and has been validated against other Navier-Stokes codes and experiments. Neither code has been used to investigate a geometry as complex as the BERP blade.

3.2 Grid Generation

To utilize CFD methods, the 3-D space surrounding the blade surface and the surface itself are divided into a structured grid system of discrete points. The physical phenomena modeled by each method places different requirements onto the grid, as shown in figure 3. Grids for viscous methods require highly concentrated number of grid points orthogonal to any body surface to capture the inherently thin viscous regions. In contrast, inviscid grids do not need high clustering at the surfaces.

The surface grids for the inviscid and viscous methods were based on a digitized database, provided by Westland, containing the BERP surface coordinates (figure 4). The interactive surface grid generation code of Steinbrenner [8] known as GRIDGEN2D was used to redistribute the spanwise locations of the Westland BERP surface coordinate database. The surface grid generation code allowed for a surface grid that conformed to a number of constraints imposed by the computational methods:

1. It must accurately represent the shape of the blade with a minimum of discontinuities.

2. Its layout should consider the overall flow-field grid topology to avoid discontinuities in the field grid.

3. Surface grid points should be concentrated according to the expected flow physics such as tip vortex formation and sharp leading-edge suction peaks.

INVISCID GRID
80 X 45 X 25

VISCOUS GRID
189 X 72 X 51
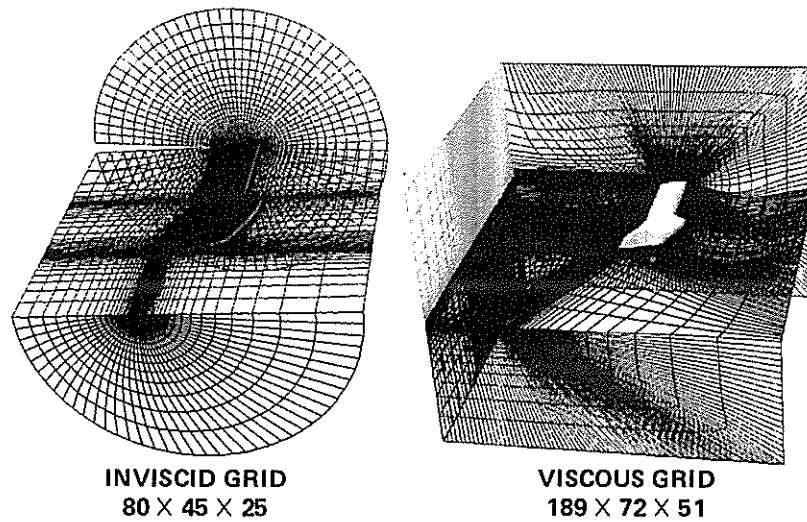
Figure 3 - Flow field grids

INVISCID GRID
80 X 33

WESTLAND
DATABASE
181 X 91

VISCOUS GRID
141 X 52
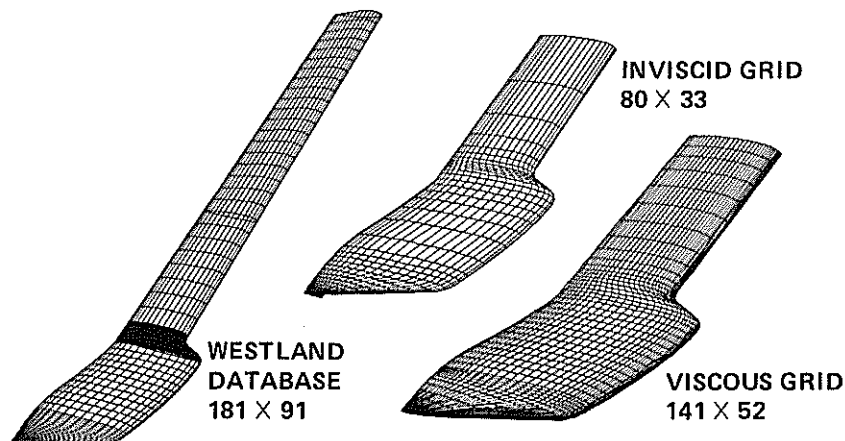
Figure 4 - Surface grids

To comply with these constraints, the spanwise locations along the leading-edge and trailing-edge of the blade were determined using GRIDGEN2D. Once these coordinate locations were found, a cubic spline routine was then used to reinterpolate the locations of the database to the desired surface points. The desired surface points were described by curves that passed through the specified leading-edge and trailing-edge locations found with GRIDGEN2D. Figure 4 illustrates the inviscid method surface grid point distribution which consists of 33 parallel sections in the the spanwise direction and 80 points distributed along each parallel section. The sections collapse to a zero thickness airfoil at the extreme tip. The viscous grid contains 52 spanwise sections each containing 141 points. The sections were distributed parallel to each other until the extreme swept tip part of the blade where the sections were slightly rotated clockwise to allow the surface grid to collapse to a singular point (airfoil of zero thickness and chord) at the blade tip.

The flow-field grids were generated with elliptic grid-generation methods first developed by Thompson [9]. In this method, a system of Poisson's equations are solved whose results describe the nodal grid points suitable for computational methods. For the inviscid method, the grid was formed by solving at each spanwise location the two-dimensional (2-D) Laplace equations. This method formed an O-H topology grid that contained 80 points in the chordwise directions, 45 points in the spanwise and 25 points radial to the body totaling 91,125 grid points.

Viscous grids require much greater control to concentrate the points near the surfaces, hence the 3-D Poisson solver by Sorenson [10] known as 3DGRAPE was used to form a C-H topology grid. First, 3DGRAPE was used to generate a coarse grid totaling 189 points in the chord direction, 72 points in the spanwise direction and 20 points radial to the blade surface with the distance of the first point off the body equal to 0.05 chords. Then, to obtain the required concentration of points, an exponential stretching function by Vinokur [11] and a cubic spline routine was used to reset the distance of the first point off the body to 0.00005 chords and to increase the number of grid points. The number of nodal grid points of the final viscous grid totaled 189 x 72 x 51 or 694,008 in total.

3.3 Flow Conditions

By taking into account the computational cost and flow limitations of the inviscid and viscous approaches, computations were performed to analyze the effects of angle of attack and Mach number shown in figure 5. The angle of attack sweep from 0^0 to 20^0 in 3^0 increments at freestream Mach number of 0.2 corresponded to Westland's experimental flow conditions. The alpha sweep was designed to overlap the CFD methods at the lower angle of attacks for code-to-code comparison and to use the viscous method at the higher angles of attack where the flow separates (a strongly viscous phenomenon). To investigate the effect of Mach number, a Mach number sweep at 6^0 angle of attack from Mach numbers of 0.2 to 0.85 was performed. Beyond 0.6 Mach number, the shock strength became too large and only the viscous approach was used. The Reynolds number, based on the freestream velocity and root chord length, equaled $1.5x10^6$ for the 0.2 Mach number case and $8.5x10^6$ for the 0.85 Mach number case. In the discussion to follow, the results will be presented in the three highlighted flow regimes shown in figure 5: low angle of attack, high angle of attack and transonic.
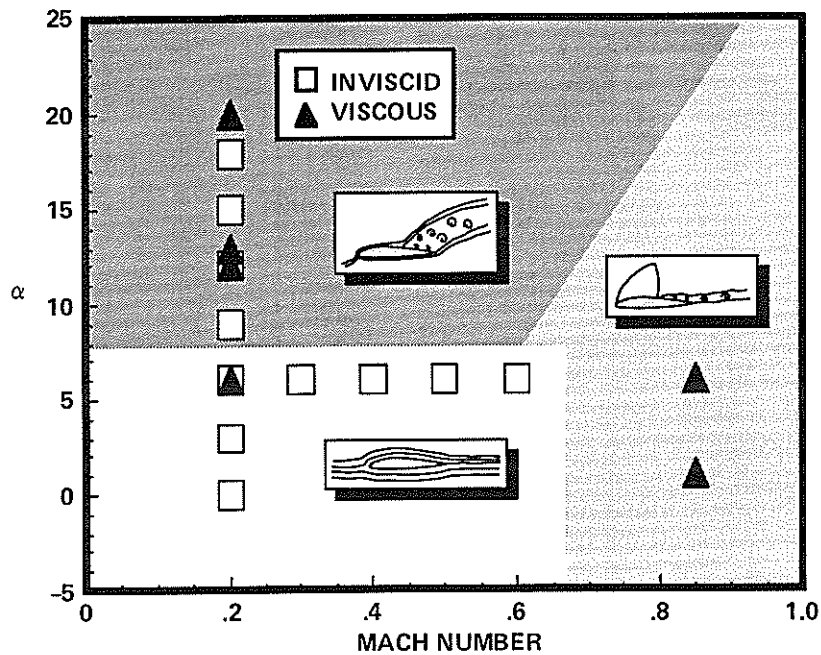
Figure 5 - Computed flow conditions

In addition to the BERP planform calculations, a rectangular planform, a sweep-taper planform, a 3:1 taper blade with the taper at 90% radius, and a Puma blade planform [12] each with the same airfoils, span and twist as the BERP blade were evaluated using the inviscid method. An angle of attack sweep at 0.2 Mach number and some transonic calculations were performed with these supplementary planforms. Figure 6, illustrates the various planforms.

4. Validation with Experiments

To gain confidence in the computational results, oil flow patterns, pressure distributions and lift are compared to the experimental data of Brocklehurst [5]. Figure 7 compares the experimental surface oil flow patterns with natural boundary layer transition to the simulated surface oil flow patterns computed by the viscous approach at M= 0.2, α=13°, and Re= 1.5 x 10^{6} with turbulence modeling; the simulated oil flow patterns were computed by releasing fictitious particles into the computed flow field close to the blade surface and confining those particles to remain close to the surface. In comparison, the trailing-edge separation evident in the experiment inboard of the notch and its disappearance outboard of the notch is captured in the computed oil flow. Also, the tip vortex of the computed and experimental flows compare quite well. The one main difference between the two is the extent of the separation region just inboard of the notch region. But, in general there is good agreement between the computed and experimental surface oil flows.

Figure 8 illustrates the comparison between four representative experimental and computed surface pressure coefficient distributions at M= 0.2, α=13°, and Re= 1.5 x 10^{6}. There is excellent agreement with the experiment at the inboard section, notch and sweep spanwise locations. At these sections, the pressure peaks and general shape of the pressure plots agree extremely well with the experiment. At the inboard location, the experimental points slightly disagree with the computed pressures toward the last 5% of chord indicating the difference in the extent of the separation found in the surface oil flow. The pressure distribution at the extreme tip, however, does not agree very well with the experiment. The computed pressure shows a vortex structure forming inboard of the leading-edge not evident in the experiment.
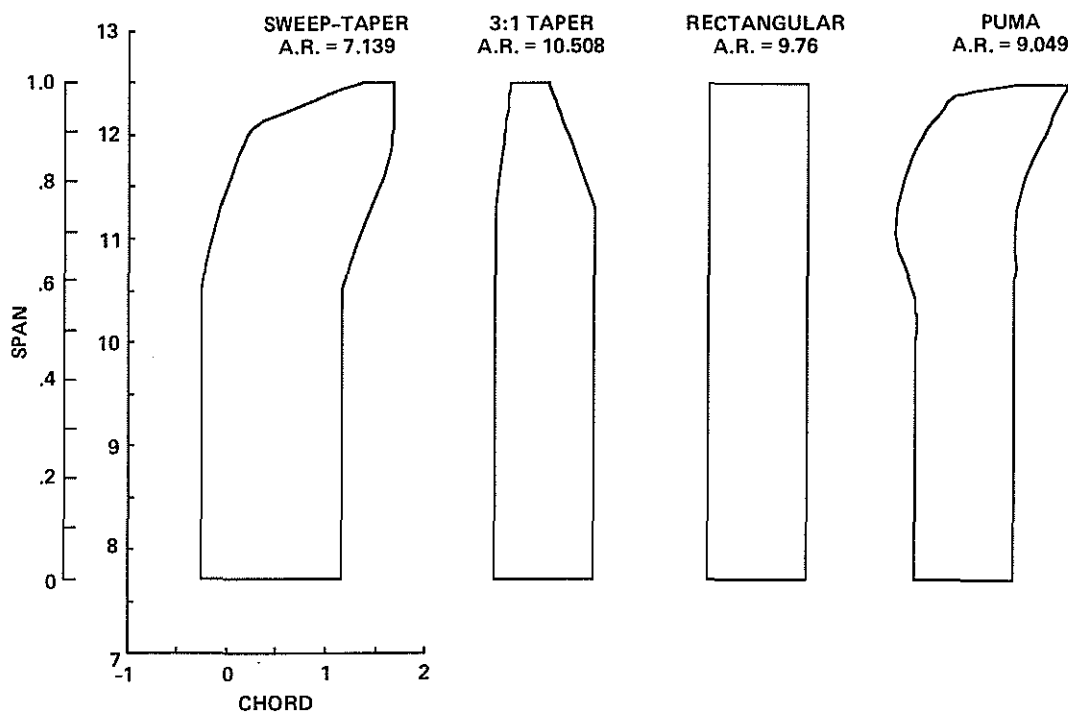
Figure 6 - Supplementary planforms

0-7

$$M = 0.2, \; \alpha = 13°, \; Re = 1.5 \times 10^6$$
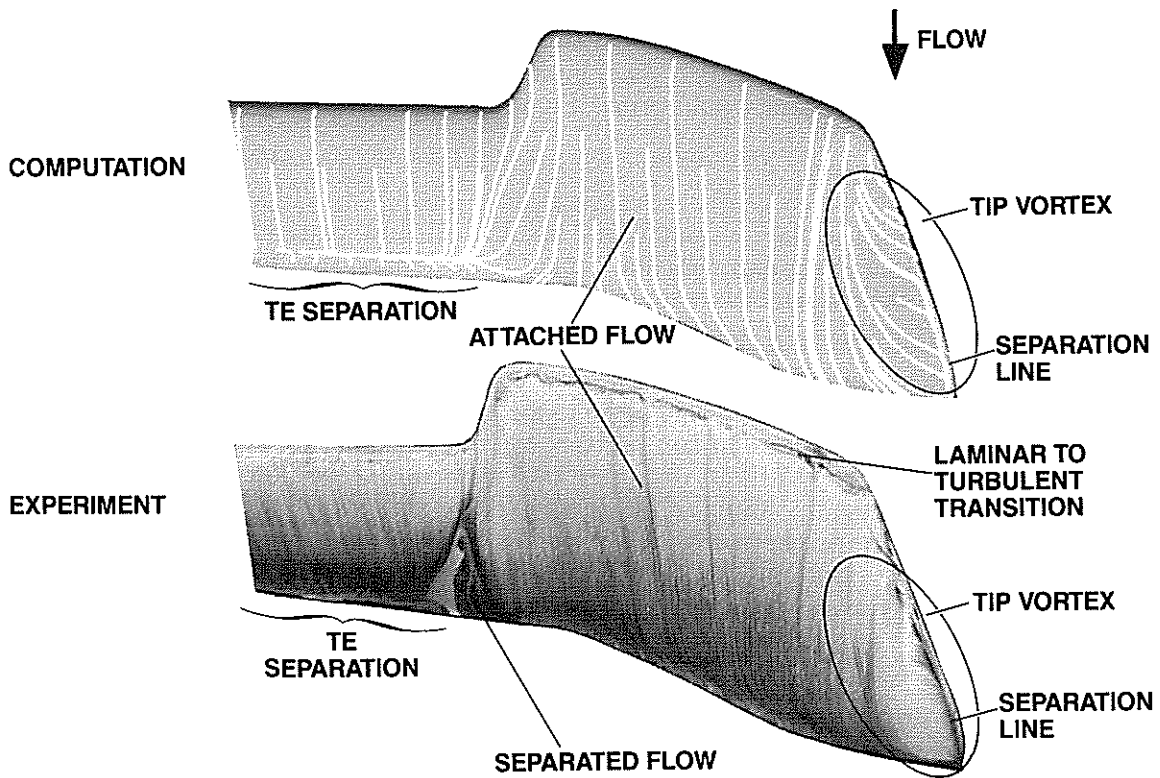
Figure 7 - Surface oil flow validation

$$M = 0.2, \; Re = 1.5 \times 10^6, \; \alpha = 13°$$
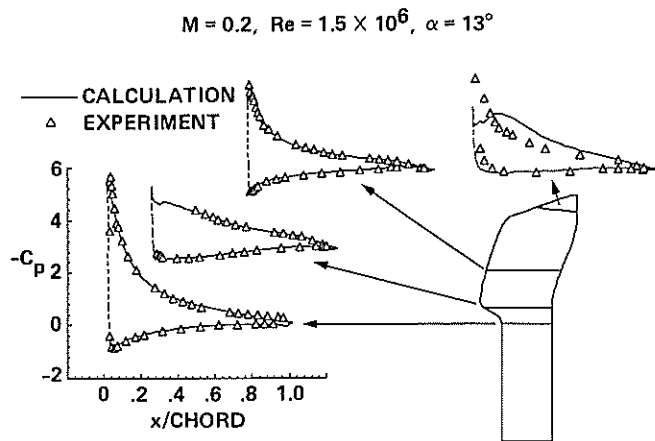
Figure 8 - Surface pressure validation

This difference indicates that at the blade's highly swept region, the tip vortex formed further inboard than in the experiment. Overall, there is excellent agreement between the computed and measured surface pressures.

Figure 9 illustrates the comparison of the experimental and computed local lift coefficient (C_l) distribution at M=0.2 and at angle of attacks of $6°$, $13°$, $16°$ and $20°$. The Reynolds
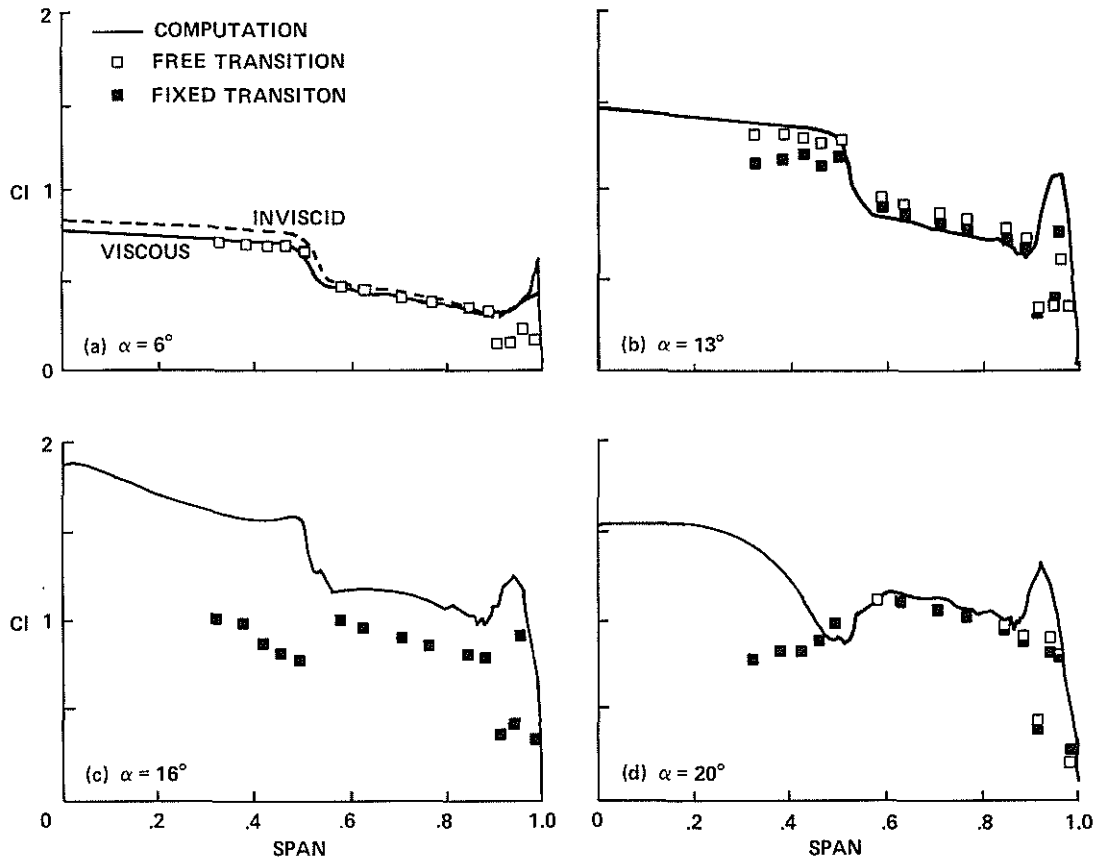
Figure 9 - Local lift coefficient distribution validation

number at 6° and 13° angle of attack is 1.5×10^6 while at 16° and 20° the Reynolds number is 1.0×10^6. The experimental data for the transition free and the transition fixed cases are shown while all the viscous computations assume fully turbulent from the leading edge. At 6°, the inviscid computation is included for added comparison between the computational methods.

As expected from the pressure comparisons, there is excellent agreement between the computation and experiment for the cases when the flow is attached such as 6° and 13°. The discrepancies between the experiment and computations occur when the blade begins to stall along the sections inboard of the notch. At the extreme tip there is some disagreement between the computation and experiment in the prediction of the tip vortex with the computation predicting a stronger tip effect than shown in the experiment. In the dataset, there are two experimental points that consistently disagree with the computation that lead one to question their reliability

Finally, the computed total integrated lift coefficients are compared to the transition free and transition fixed experimental data as shown in figure 10. As expected from the earlier comparisons, the lift coefficients compare well at the predominantly attached flow cases. At high angles of attack, there is a difference between the two sets of experimental data because the boundary layer trip was optimized for the 13° case. The experiment and computation at 16° and 20° disagree because of the discrepancy in the amount of separation indicated in figures 9c and 9d.

These comparisons now give confidence to the computations. They place bounds on the following discussion and highlight areas where the computations may lead to erroneous conclusions. These comparisons also illustrate the capability of CFD to provide additional data
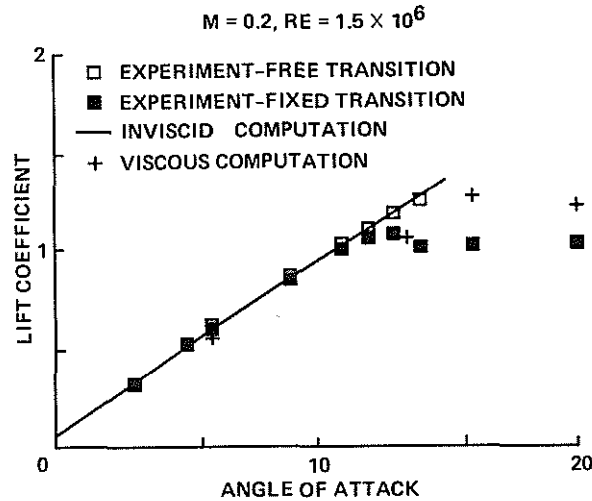
Figure 10 - Integrated lift coefficient validation

to complement experimental data and they now allow conclusions to be drawn regarding the aerodynamic characteristics of the BERP blade.

5. Results

5.1 Low Angle of Attack Case

At low angles of attack, the BERP blade exhibited greater induced drag at a given lift than the sweep-taper, the rectangular, and the Puma. However, the BERP exhibited less induced drag than the 3:1 taper planform. Figure 11 illustrates the induced drag polar comparison between the BERP and the other planforms as computed by the inviscid method at M=0.2. The induced drag polar for the non-BERP planforms were corrected to the BERP blade aspect ratio.

As a check on the computed induced drag, the computed results for a NACA 0012 untwisted rectangular wing is compared with linear wing theory as given by equation (1).

$$C_D = C_L^2 \frac{(1 + \delta)}{\pi A.R.}$$

Where:
C_D = Integrated Drag Coefficient
C_L = Integrated Lift Coefficient

δ = correction factor
A.R. = Aspect ratio

(1)

The correction factor, δ, in equation (1) for a 12% thick rectangular planform wing as given in Perkins and Hage [13] yields a drag polar slope of 0.0411. The slope for the computed untwisted rectangular case is 0.04598 at a Mach number of 0.2 or 0.04411 when corrected to a Mach number of 0.0 using the Prandtl-Glauert factor.

The low angle of attack results also lead towards an understanding of the aerodynamic characteristics at the more extreme flow conditions. Figure 9a illustrates the comparison of the computed and experimental local lift coefficient at $\alpha = 6^\circ$ and M=0.2. The variation in the local lift coefficient is primarily a result of the planform chord variation. For example, the increase
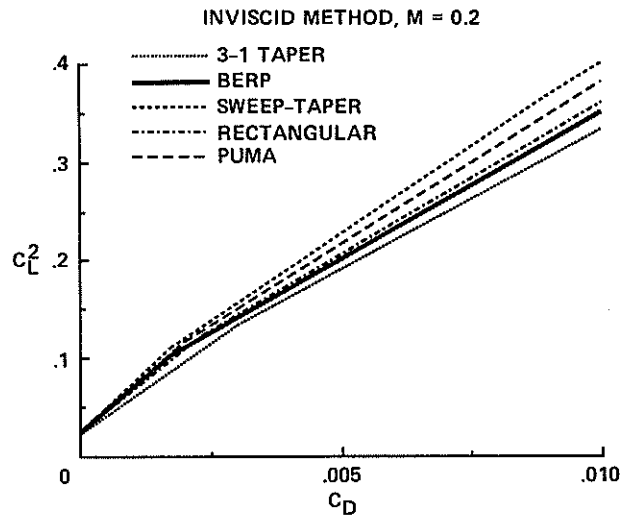
Figure 11 - Induced drag polar comparison

in chord at the sweep section of the BERP causes a drop in C_l. While at the extreme tip, the C_l begins to increase resulting from the decrease in local chord. In addition, the viscous computation shows evidence of vortex lift indicated by the difference in the lift coefficient between the inviscid and viscous computation. These characteristics show that the swept region of the BERP blade will remain attached much longer than the inboard sections. This behavior comes from the basically two-dimensional idea of reduced local lift coefficient from planform change and the three-dimensional effect of vortex lift.

Figures 12a and 12b further compares the BERP local lift and induced drag coefficients at $\alpha = 6^{\circ}$ and M=0.2 to the non-BERP planforms. In comparison to the other planforms, the local lift coefficient of the BERP is the only one that exhibits a significant drop at span locations greater than 0.5. This again illustrates the blade's capability to reduce the onset of separation as compared to other planforms; the other planforms tend to maintain higher C_l. At the notch section, span location of .5, the BERP blade exhibits a large negative induced drag force that results from a large leading edge suction peak at these sections. At higher angles of attack, this behavior will tend to cause the boundary layer to prematurely separate from the leading edge and at transonic speeds it can cause local pockets of high Mach number flow.

5.2 High Angle of Attack Case

At high angles of attack, the BERP blade exhibits the ability to attain high lift coefficients by maintaining attached flow in the sweep part of the blade. Figure 10 illustrates the integrated lift coefficient (C_L) versus angle of attack for the BERP blade as computed by both CFD methods at a M=0.2 and Re= 1.5 x 10^6. First, at α= 13°, 16° and 20°, the viscous solutions diverge from the nearly linear increase in lift as predicted by the inviscid method. This difference illustrates the presence of separated flow and the need for a viscous method to capture this flow feature. Secondly, at α= 16° and 20° , the lift has reached a plateau where as one would expect the blade to stall with a drastic drop in the lift at approximately α=12° to 15°.

The blade attains high-lift by maintaining attached flow at the outer spanwise locations. Unrestricted particle traces shown in figure 13 illustrate the predicted flow around the blade at α= 20°, M=0.2 and Re=1.5x10^6. The traces indicate a highly separated flow shown as a large vortical structure fixed over the inboard sections. A leading edge stalled region then forms just inboard of the notch region. The flow remains attached at the sweep region of the blade with a tip vortex at the extreme edge.
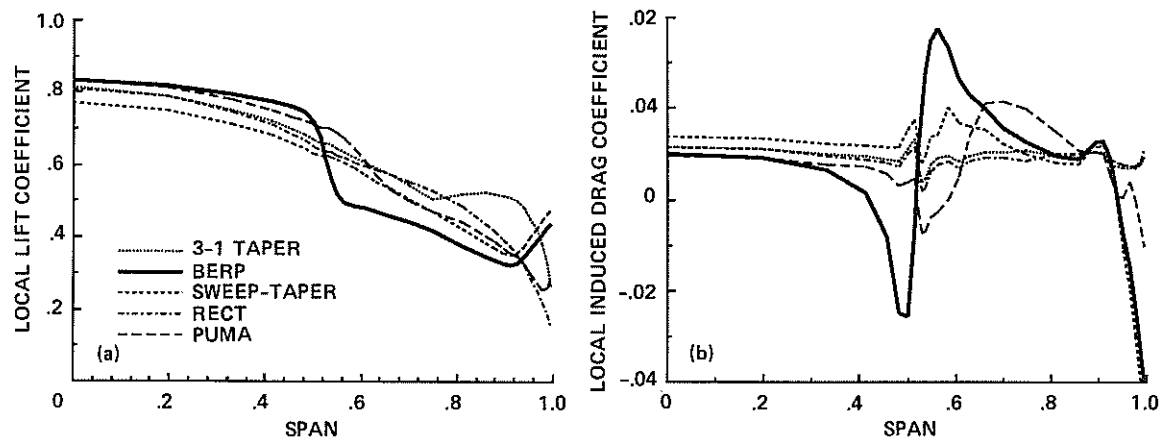
Figure 12 - Local force coefficient comparison

$$M = 0.2, \quad \alpha = 20°, \quad Re = 1.5 \times 10^6$$
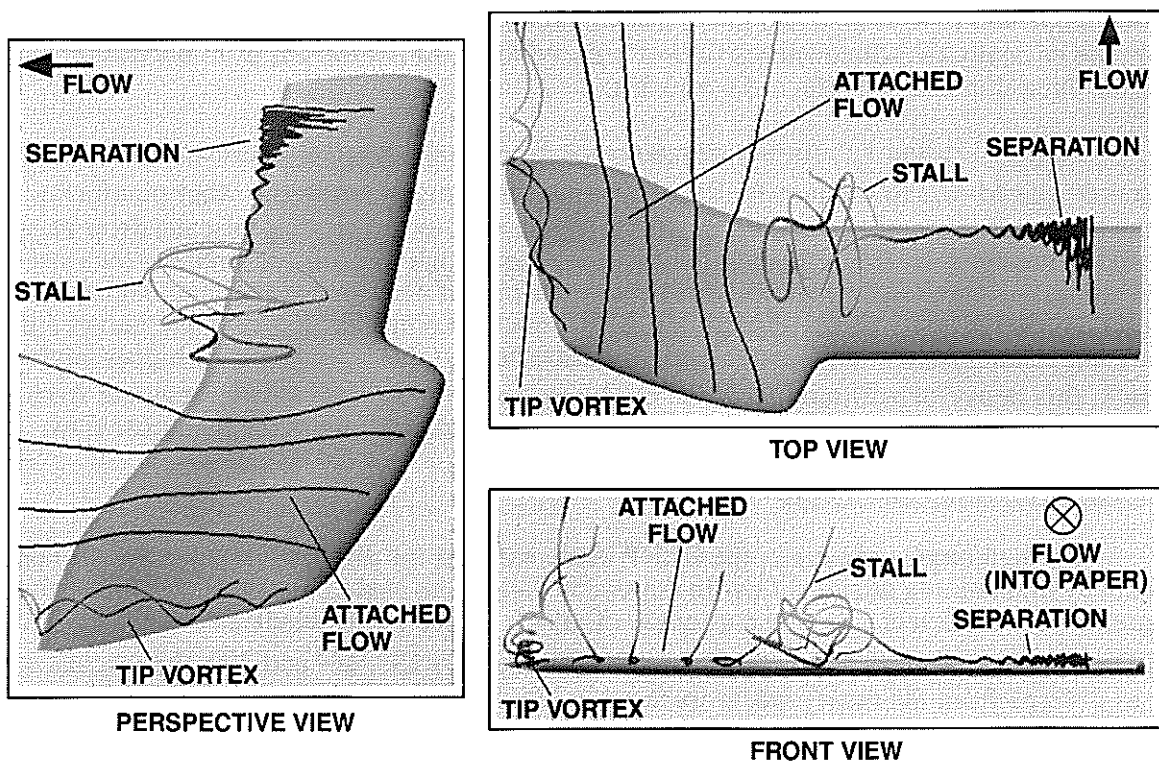
Figure 13 - Unrestricted particle traces

The simulated surface oil flow pattern, shown in figure 14, further illustrates the blades ability to maintain attached flow at the outer span. Inboard of the notch, the flow separates at approximately 1/3 chord with the flow separating from the leading-edge at the beginning of the notch region. A complex separation pattern exists behind the primary inboard separation line which includes a number of secondary separation and reattachment nodes and a dominant reattachment node at the notch region. Beyond the notch, the simulated oil pattern exhibits a predominantly attached flow which has some separation towards the trailing-edge. Finally, a tip vortex appears at the highly swept extreme edge.

The blade's separation behavior directly affects the spanwise load distribution. Figures 9b and 9d illustrate the local C_l spanwise distribution for the $\alpha=13^o$ and 20° cases as computed with the viscous method. The C_l distribution at $\alpha=13^o$, a predominantly attached flow, shows a drop in the C_l beyond the notch region with an increase in C_l from the tip vortex and local chord decrease at the extreme spanwise location. In contrast, the 20° case has a drop in C_l at the notch with an increase at the swept region resulting from the flow reattachment.

For a blade in rotation, the BERP's high angle of attack capability can increase rotor thrust by allowing the advancing blade to provide more lift since the retreating blade can maintain a higher total lift coefficient. The computations showed that the blade geometry maintains attached flow beyond the notch and prevents separated flow from penetrating beyond the notch. The last 15% radius of the blade provides a large majority of the blade lift in comparison to the inboard blade sections.

5.3 Transonic Case

At transonic speeds the BERP geometry has a dramatic effect on the extent of supersonic flow and shock strength on the blade. Figure 15 illustrates the comparison of inviscid upper surface Mach contours of the BERP, the rectangular, 3:1 taper, Puma and sweep-taper planforms at $\alpha=6^o$, $M=0.6$. These computations were performed at the same aspect ratio and span. As shown by the heavy black line which delineates the boundary between subsonic and supersonic flow, the rectangular, swept-taper and 3:1 taper planforms' supersonic pockets extend much further in the spanwise direction as compared to the BERP and Puma. In short, only the BERP and Puma blade with the forward sweep or leading edge notch configuration significantly reduced the supersonic regions in the outer span.

The capability to decrease shock strength at the blade tip greatly affects the wave drag on the blade. To investigate the planform effect on the wave drag, the local wave drag coefficient was approximated by taking the difference between the local C_d at $M=0.6$ and $M=0.2$; this difference is defined as C_{diff}. Figure 16 shows that in comparison to the other planforms, the sweep-taper and the BERP have lower C_{diff} at span locations greater than 0.75; the 3:1 taper has the largest C_{diff} values at these locations. Between span location of 0.5 and 0.6 (the BERP notch location), the BERP has a very large variation in C_{diff}. Also, the BERP has the largest C_{diff} values between span locations of 0.55 to 0.75.

At higher Mach numbers, the decrease in the extent of the supersonic zone has a dramatic effect on the shock-induced separation. Figure 17 illustrates the pressure coefficient contours on the upper surface of the BERP blade at a Mach number of 0.85, a Reynolds number of 8.5×10^6, and angles of attack of 6° and 1°. As in the previous inviscid computation, the viscous computations show that the shock-strength dissipates beyond the notch, indicated by the diminished concentration of contours lines at the sweep section of the BERP. The reduction in the shock strength directly influences the extent of the shock-induced separation as shown in figure 18. The flow on the blade is separated inboard of the notch while ,beyond the notch, the flow remains attached because of the reduced shock strength.

$$M = 0.2, \quad \alpha = 20°, \quad Re = 1.5 \times 10^6$$
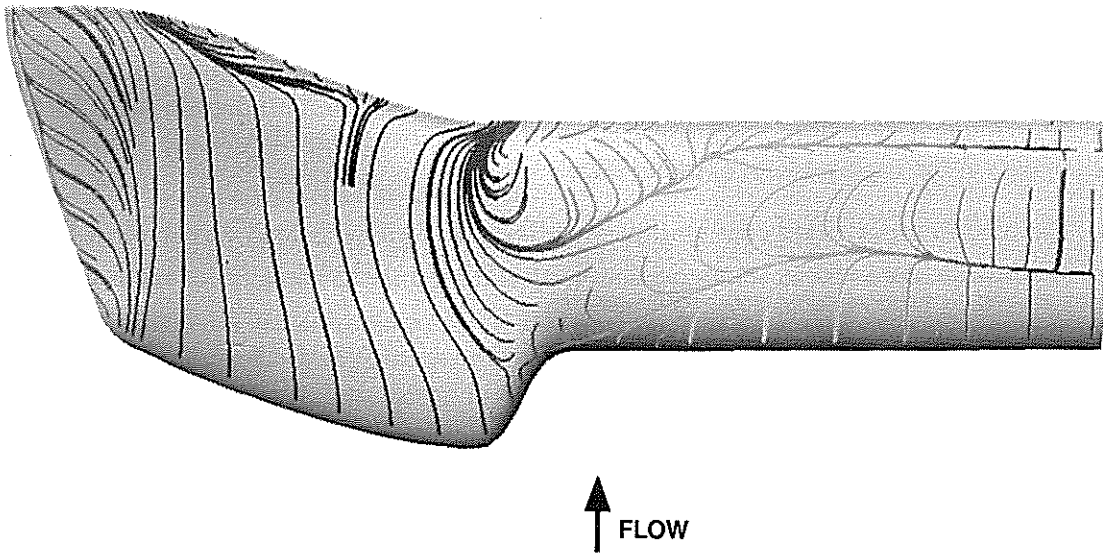
FLOW

Figure 14 - Simulated surface oil flow

$M = 0.6°, \quad \alpha = 6°, \quad$ INVISCID METHOD, SURFACE MACH CONTOURS

FLOW ⟶
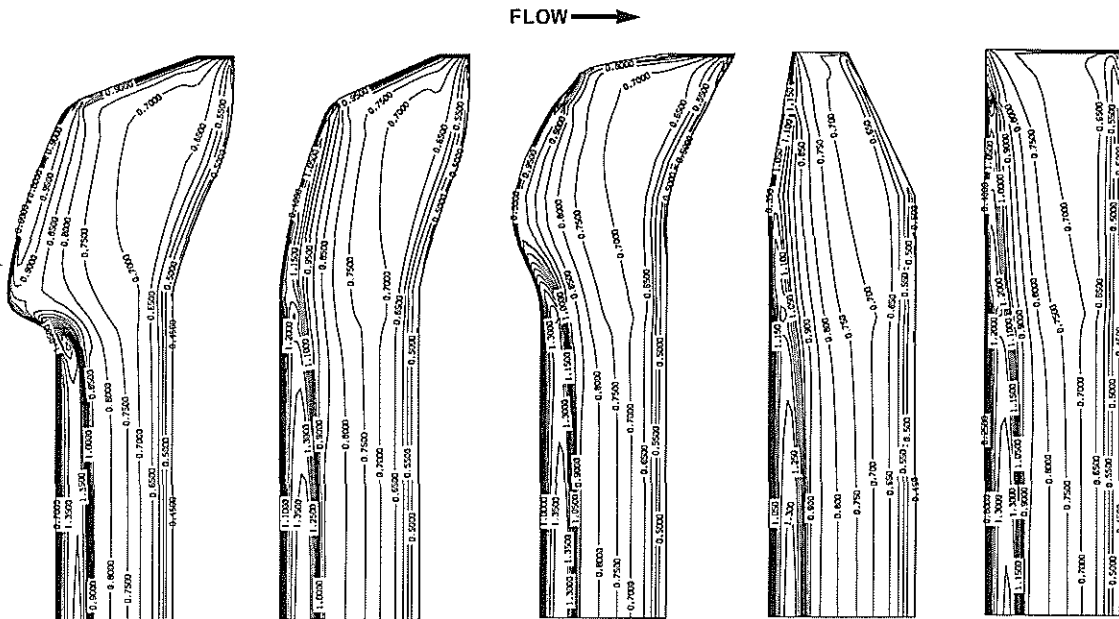
Figure 15 - Planform effect at transonic speeds

INVISCID METHOD, $\alpha = 6°$
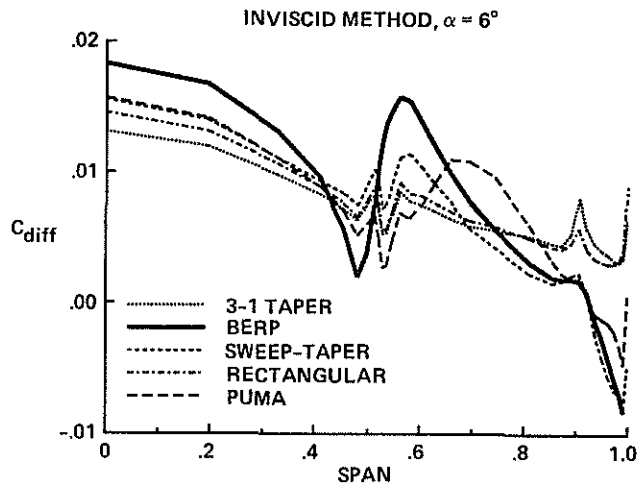
Figure 16 - Comparison of $C_{diff} = [\ C_d(M=0.6) - C_d(M=0.2)\ ]$

$M = 0.85$, $Re = 8.5 \times 10^6$

1 DEGREE

6 DEGREE

FLOW
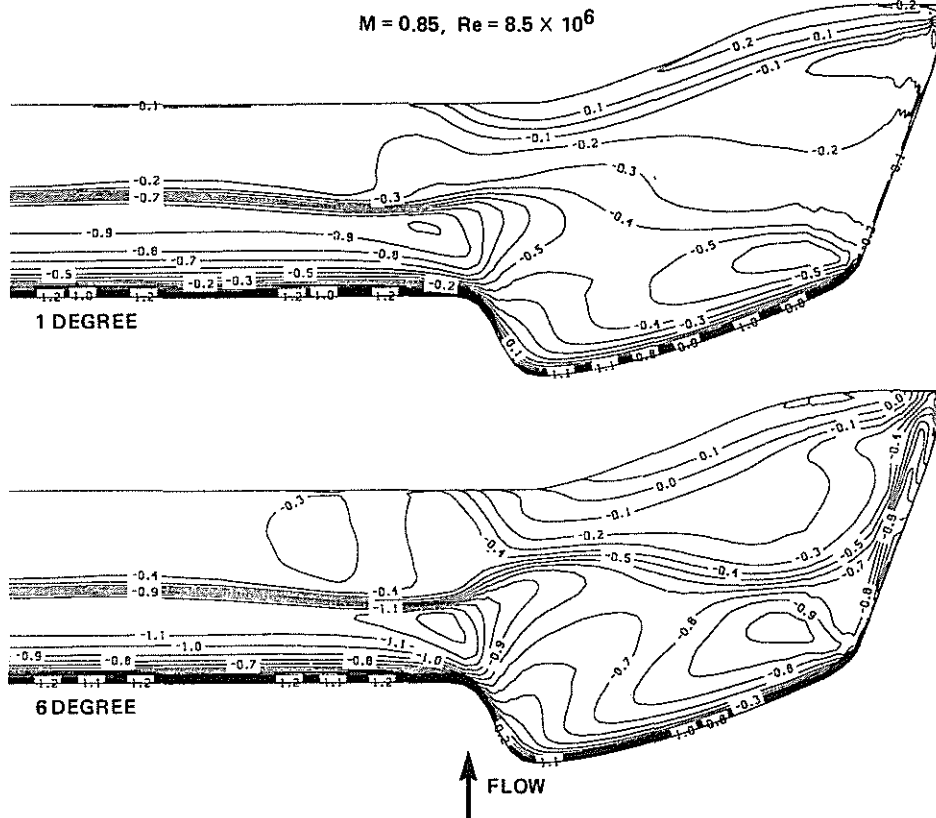
Figure 17 - Surface pressure coefficient contours

$$M = 0.85, \ Re = 8.5 \times 10^6$$

1 DEGREE

6 DEGREE

FLOW
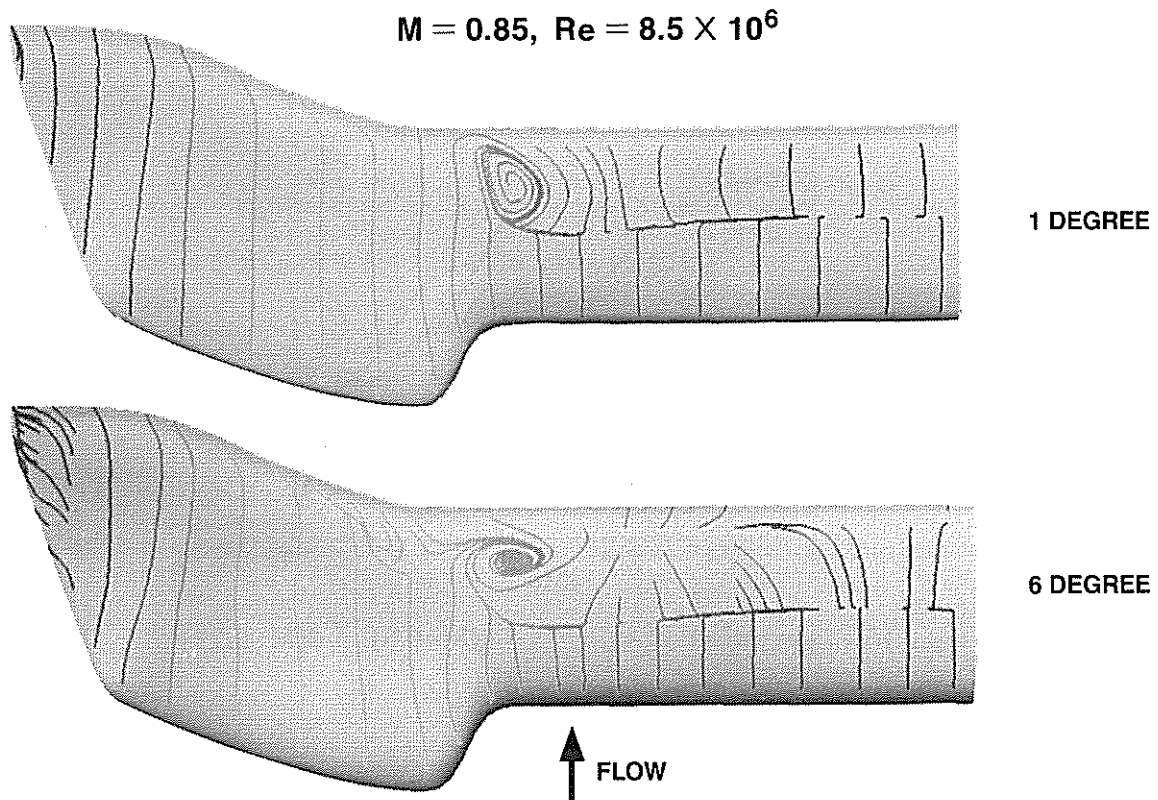
Figure 18 - High speed separation patterns

In summary, the nonrotating transonic results imply some favorable and unfavorable characteristics of the BERP blade in rotation. One, the BERP will require less power to overcome wave drag at high transonic tip speeds as compared to other rotor blades such as rectangular, taper and other swept tips. But, the C_{diff} values around the vicinity of the notch were higher than other planforms. This behavior detracts from the BERP's reduced C_{diff} at the more extreme span locations. Secondly, the reduction in shock strength in the spanwise locations beyond the notch greatly reduces the amount of shock-induced separation on the BERP. This behavior would reduce the amount of power required and help to alleviate the amount of vibrations and control loads on the blade.

6. Conclusions

In conclusion, the nonrotating computations in this study have increased the fundamental understanding of the BERP blade's aerodynamic properties. They have shown how the blade's unique combination of airfoils and planform shape affect the blade loads and how these nonrotating characteristics may influence the rotating blade performance. Specifically, at low angles of attack, the BERP exhibited greater induced drag for a given lift as compared to some other types of planforms. This characteristic implies that the induced power requirement for the BERP in a rotating flow environment would be higher in comparison to the rectangular, Puma or sweep-taper planforms but less for a 3:1 taper blade planform. At high angles of attack, the BERP can attain higher C_L by minimizing separation on the outer spanwise locations. This capability can increase the available rotor thrust by allowing the advancing blade to provide more lift. In addition, the leading-edge notch and tip sweep combination significantly reduces the transonic effects on the blade that sweep alone cannot accomplish. The milder transonic effects would reduce the power required to overcome wave drag and reduces the control loads and vibrations generated by shock-induced separation at high tip speeds.

7. Acknowledgements

8. References

[1] Harvey, D., " The Hind D Close Up: Ivan's Evolving Gunship", Rotor and Wing International, pg 48, May 1988.

[2] Perry, F.J., " Aerodynamics of the Helicopter Speed Record", 3rd Annual National Forum of the American Helicopter Society.

[3] Hansford, R.E., " Rotor Load Correlation with the British Experimental Rotor Program Blade", Journal of the American Helicopter Society, Volume 32, Number 3, July 1987.

[4] Wilby, P.G., " An Experimental Investigation of the Influence of a Range of Aerofoil Design Features in Dynamic Stall Onset" 10th European Rotorcraft Forum, The Hague, The Netherlands, Aug,1984.

[5] Brocklehurst, By personal communication, November 1988.

[6] Strawn, R.C., and Caradonna, F.X., " Conservative Full Potential Model for Unsteady Transonic Rotor Flows", AIAA Journal, Vol. 25, No. 2, pg. 193, February 1987.

[7] Obayashi, S., Fujii, K., and Gavali, S., " Navier-Stokes Simulation of Wind-Tunnel Flow Using LU-ADI Factorization Algorithm", Numerical Simulation of the Transonic DFVLR-F5 Wing Experiment, Proceedings of the International Workshop "Numerical Simulation of Compressible Viscous-Flow Aerodynamics", September 30 - October 2, 1987, Gottengen, FRG, Notes on Numerical Fluid Mechanics, Volume 22, Friedr.. Vieweg & Sohn, Braunschweig/Weisbaden, 1988.

[8] Steinbrenner, J.P., " GRIDGEN2D (Interactive Elliptic Surface Grid Generator), User's Manual", CFD Report # 063-4-8601, General Dynamics, Fort Worth Division, June 13,1986.

[9] Thompson, J.F., Thames, F.C. and Mastin, C.W., " Automatic Numerical Generation of Body-Fitted Curvilinear Coordinate System for Field Containing Any Number of Arbitrary Two-Dimensional Bodies", Journal of Computational Physics , pg 299-319, 1974.

[10] Sorenson R.L., " Three-Dimensional Zonal Grids About Arbitrary Shapes by Poisson's Equation", Proceedings of the 2nd International Conference of Numerical Grid Generation in Computational Fluid Dynamics , Pineridge Press, Swansea, U.K., 1988.

[11] Vinokur, M., " On One-Dimensional Stretching Functions for Finite-Difference Calculations", Journal of Computational Physics , Vol. 50, 1983.

[12] Riley, M.J.and Miller J.V., " Pressure Distributions on a Helicopter Swept Tip from Flight Tests and form Calculations", 9th European Rotorcraft Forum, Stresa, Italy, September 1983.

[13] Perkins, C. and Hage, R., Airplane Performance, Stability and Control , John Wiley & Sons, London, pg. 74, 1949.